Microwave-driven synthesis of bisphosphonate nanoparticles allows *in vivo* visualisation of atherosclerotic plaque.

J. Pellico[a,b], A.V. Lechuga-Vieco[a], M. Benito[a], J.M. García-Segura[b], V. Fuster[c], J.Ruiz-Cabello[a,b], F. Herranz[a*].

A fast and reproducible microwave-driven process has allowed us to synthesise Neridronate-functionalised nanoparticles. Contrary to traditionally the phosphate groups decorate the outside layer of the particles providing Ca^{2+} binding properties *in vitro* and selective accumulation *in vivo* in the atheroma plaque. *In vivo* and *ex vivo* detection by T_2-weighted MRI is demonstrated and validated by histology. The accumulation in the plaque takes place in less than one hour since the intravenous injection, which is particularly suitable for clinical applications.

The use of iron oxide nanoparticles (IONP) in biomedicine is a well-established and vast field encompassing from drug-delivery to hyperthermia and clinical diagnosis of several diseases.[1,2] Lately there has been an increasing deal of attention to the use of microwaves synthesis (MWS) for the production of high quality nanoparticles of different composition. MWS dramatically reduces reaction times, increase yields and enhances reproducibility, parameters of critical importance for the synthesis of IONPs.[3–5] MW technology allows for a fine-tuning of the main parameters affecting the behaviour of IONPs. This way ultrasmall nanoparticles (<10 nm) or larger ones (20-100 nm) can be easily obtained.[5–8] This flexibility is also clear in the synthetic methodologies than can be used, from coprecipitation to thermal decomposition, as we demonstrate here.[9,10] Bisphosphonates (BiP) are chemically stable derivatives of inorganic pyrophosphate (PPi) and have been used in the clinical practice for more than three decades.[11] Bisphosphonates are used to treat a wide variety of conditions because of, like their natural analogue PPi, their high affinity for bone mineral, binding to hydroxyapatite crystals.[11] BiP molecules have been previously used for their binding properties towards the Fe_3O_4 surface.[12–14] Here we propose a radically different approach; to decorate the outer layer of the particle rather than attach to the surface to keep the calcium binding properties of these functionalities and target the atherosclerosis plaque. Neridronate (Scheme 1) is a BiP with five methylene units and a final free amino group, particularly well suited for the functionalisation of the carboxylic groups on the surface of the nanoparticles.

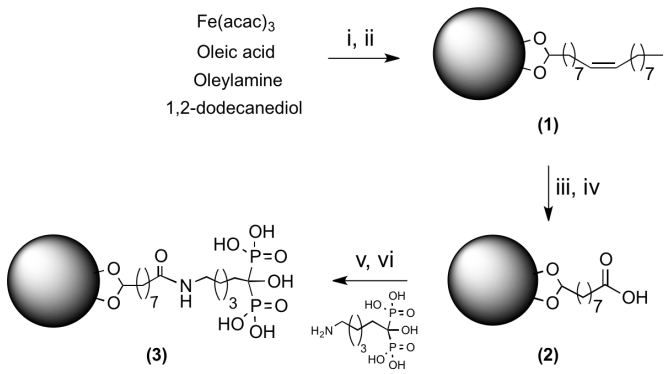

Scheme 1. Synthesis of neridronate functionalised nanoparticles (**3**). Reagents and conditions: (i) 60 ºC, 2 min.; (ii) 180 ºC, 20 min.; (iii) KMnO4, BTACl, 105 ºC, 300 W, 9 min.; (iv) pH 2.9, 105 ºC, 300 W, 9 min.; (v) EDC, sulfo-NHS, pH 7.0, 30 min.; (vi) HEPES pH 7.7, 2 h.

Atherosclerosis is an inflammatory pathology of the blood vessel wall in which plaque builds up inside the arteries. Plaque is mainly made up of lipids, cholesterol, calcium, macrophages and several substances found in the blood. Over time, plaque hardens and narrows the arteries, limiting the flow of oxygen-rich blood to the organs. The acknowledgment of the importance of this pathology from a global health and economical point of view has motivated a great deal of research for the early diagnosis of the plaque by non-invasive techniques.[15,16] The specific targeting of the plaque can be addressed with several biomarkers like metalloproteinases, LDL-oxidised, calcium vesicles, receptors involved in neoangiogenesis or macrophages.[17–19] The aim of this work was to use MWS for the production of high-quality biocompatible nanoparticles and to functionalise them with neridronate. Our hypothesis was that the Ca^{2+} binding properties of this group would provide *in vivo* targeting towards the calcium vesicles in the atheroma plaque and therefore be of use for an easy diagnosis of atherosclerosis plaque.

Oleic acid–coated iron oxide nanoparticles (OA-IONP) were synthesised in the microwave by a modification of published protocols.[20] Briefly, a mixture containing $Fe(acac)_3$, oleic acid, oleylamine and 1,2-dodecanediol in benzyl alcohol was stirred at 60ºC for 2 min at 300 W. After that, the temperature was increased from 60ºC to 180ºC and stirred during 20 min (Scheme 1). As typically occurs when using MWS (Discover SP, CEM), due to the very fast heating, the NPs can be synthesised with very small size. The core size, by Transmission Electron Microscopy (TEM), for the very homogeneous hydrophobic nanoparticles (**1**) is 3.7 ± 0.8 nm (N=50, Figure 1a). Besides high resolution TEM shows the lattice fringes on the Fe_3O_4 cores, demonstrating excellent crystallinity

(Figure 1a). The hydrodynamic size, by Dynamic Light Scattering (DLS), is also extremely small with a value of 7.5 nm (Figure 1c). The infrared spectrum of the nanoparticles (Figure S1) shows the typical bands for OA-IONP.[21] To render these hydrophobic nanoparticles stable in water we chose a direct chemical modification of the surfactant with the help of microwave technology.[21–23] The use of MWS in this modification (Scheme 1) clearly demonstrates the most important advantage of this technology, the rapidness and reproducibility of the reaction. The process was divided in two steps of 9 minutes each, first for the formation of the complexes between MnO_4^- and the olefin and the second step for the cleavage of the oleic acid molecule. The synthesis rendered Azelaic acid-IONP (**2**) with a hydrodynamic size of 30 ± 5 nm by DLS (Figure 1c), similar to the value obtained by the thermal approach. The excellent reproducibility achievable by MWS with our equipment (Discover SP, CEM) is also shown in Figure 1d. It can be seen how after four repetitions of the synthesis the same size and size distribution was obtained. The value for the zeta potential (-44 mV) at pH 7 is also in the expected range. TEM images of nanoparticles **2** show that there is no aggregation upon modification of the oleic acid structure. The core size for the hydrophilic nanoparticles is similar to particles **1**, with a value of 4.9 ± 0.9 nm (N=50, Figure S2). FTIR spectrum of nanoparticles **2** shows the expected changes due to the breaking of oleic acid chain (Figure S1). There are three modifications in comparison with spectrum for **1**; the lack of the C-H signals due to the minor number of CH_2 groups at 2854 cm^{-1} and 2925 cm^{-1}, the broadened C=O peak at 1660 cm^{-1} due to the presence of two carbonyls in the molecule and the disappearance of the signal at 1432 cm^{-1} assigned to double bond in oleic acid. On the other hand, in the spectra of **2**, at least three bands can be clearly assigned to the azelaic acid molecule at 1000 cm^{-1}, 1045 cm^{-1} and 1175 cm^{-1}. Relaxivity values for nanoparticles **2** were also measured to determine their performance as T_2-weighted MRI contrast agents. Relaxivity values were 15.3 ± 1.1 $mM^{-1}s^{-1}$ for r_1 and 90.7 ± 3.5 $mM^{-1}s^{-1}$ for r_2. These values are similar to the previously reported for the thermal synthesis. Only a slightly larger r_1 value that can be attributed to the much faster synthesis in MW and therefore smaller cores in the nanoparticle. Once nanoparticles **2** were obtained we carried out the final modification by the amide formation between the amine group in neridronate and the carboxylic groups in azelaic acid molecule. For this, traditional EDC/sulfo-NHS conjugation was used, since employing an activated carboxylate with the sulfo-NHS ensures colloidal stability during the reaction. Final magnetic purification rendered nanoparticles **3** with very good colloidal stability. The TEM images for the neridronate-functionalised nanoparticles are shown in figure 1b. It is clear the homogeneous distribution, the lack of aggregation and the crystallinity of the sample, with size of the core of 5.5 ± 0.7 nm (N=50, Figure 1b). Regarding hydrodynamic size they show an almost identical value than **2** of 40 ± 4 nm and a narrow size distribution, confirming that the whole process did not change the core of the nanoparticle and only a slightly larger hydrodynamic size is obtain as expected (Figure 1c). The incorporation of the new functional group was confirmed both by FTIR and Energy-dispersive X-ray spectroscopy (EDX) (FigureS1 and Figures S3). Infrared data show the expected changes, like a slight reduction in the wavenumber of the carbonyl band, from 1660 cm^{-1} to 1636 cm^{-1}, due to the formation of amide bonds and the presence of bands that also appear in neridronate spectrum, like those at 1179 cm^{-1} and 1043 cm^{-1}. EDX also confirms the presence of neridronate in the nanoparticle with 10.5% atomic weight of phosphorous relative to iron (Figure S3). Relaxivity values for nanoparticles **3** were also similar to those for **2**, 11.2 ± 1.7 $mM^{-1}s^{-1}$ for r_1 and 93.3 ± 3.1 $mM^{-1}s^{-1}$ for r_2. At this point we checked the Ca^{2+} binding properties of the nanoparticles due to the presence of the bisphosphonate groups. It has been previously shown that the modification in the aggregation state of the nanoparticles can be detected by changes in the relaxation time values.[24] For that a 50 μg Fe/mL solution of nanoparticles **3** was prepared and titrated with different calcium solutions (blank, 12 μM, 25 μM and 50 μM).

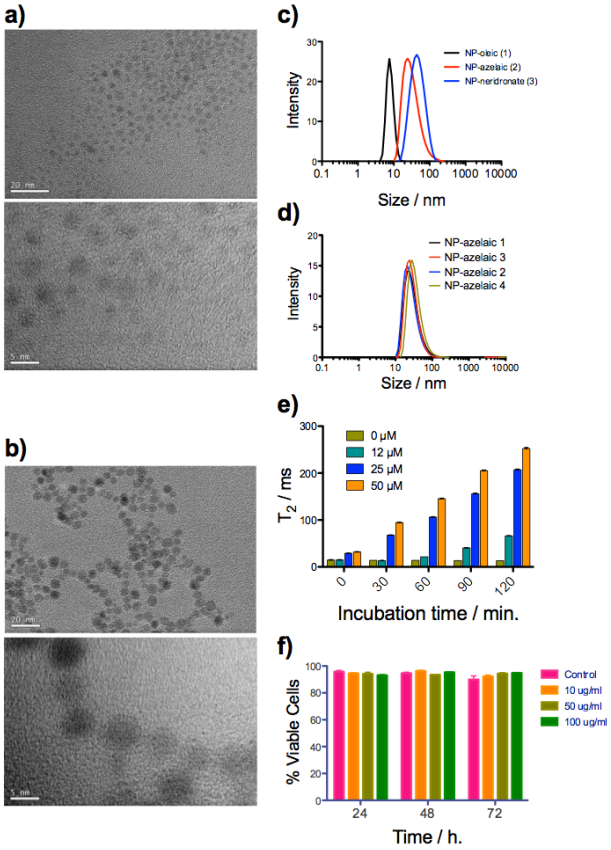

Figure 1. a) TEM images, at two magnifications, for **1**; b) TEM images, at two magnifications, for **3**; c) Hydrodynamic size for nanoparticles **1**, **2** and **3**; d) Hydrodynamic size for **2** in four different synthesis; e) Evolution of T_2 relaxation time in a solution of **3** as a function of time and calcium concentration and f) Cell viability after incubation with **3** at different concentrations and incubation time.

As figure 1e shows the value of the T_2 relaxation time increments linearly with the amount of Ca^{2+} and the time of incubation due to the formation of clusters of nanoparticles (nanoparticles in the same solution but without Ca^{2+} remained stable). These results confirm that the binding capacity of the bisphosphonate groups in **3** is not lost during the functionalisation step, as was indeed expected. This is a fundamental result since our hypothesis is that the calcium binding capacity would enable the plaque targeting capabilities through macrophage capture.[25] Cellular uptake by Mouse Adult Fibroblasts (MAFs) C57/BL6 of nanoparticles **3** was assessed by flow cytometry, by an increased side scatter (SSC) and by bright field microscopy after using Perls staining in cell culture (Figure S5).[26] SSC is increased after treatment with successively higher doses of **3** as expected with the incorporation of the nanoparticles. Increased SSC was observed in a dose dependent manner. Cell size and morphology after incubation for 24 hour, as well as the cell uptake were assessed by Perls staining confirming the incorporation of **3** in the cells. Cytotoxicity of the **3** was also checked with MAFs, cell viability and proliferation were studied for three concentrations and

three incubation times. Results are shown in Figure 1f and Figure S4 and clearly shown that there is no remarkable cytotoxicity even at such a high concentration as 100 μg/mL. For the *in vivo* MRI study ApoE$^{-/-}$ mice, 48 weeks old, were used. First, aorta and carotids basal images were taken (Figure 2a), where the formation of the atherosclerotic lesion can be clearly seen. After that, a solution of neridondronate-functionalised nanoparticles (**3**, 100 μL, 1 mg Fe/mL) was intravenously injected in mice and images were recorded one hour post injection. Figure 2a shows the plaque in the aorta pre (top) a 1h post injection (bottom). It is clear in these images that the plaque, after the injection of the particles, is hipointense in comparison to the basal images. This difference in intensity can in fact be quantified (Figure 2b) by the selection of two ROIs (region of interest) in the plaque and two in the muscle for reference. The plaque to muscle relative signal clearly shows a significative reduction in the intensity one hour after the injection of nanoparticles **3**. To confirm that this signal reduction was due to the accumulation of nanoparticles and not because of their circulation in the blood their circulation lifetime was studied. Ideally, a good contrast-enhanced nanoparticle system should accumulate rapid and specifically in the targeted area and should be cleared immediately to avoid background signal. Besides this accumulation should be as fast as possible since this would determine a higher translational power.[25,27] Nanoparticles **3** were injected (100 μL, 1 mg Fe/mL) and the signal in the liver monitored with time. It is clear in the graph that after 20 minutes the nanoparticles have cleared from circulation, ruling out any possible effect on the images (Figure 2c). To confirm these data, *ex vivo* imaging and histology were performed on the studied mice.

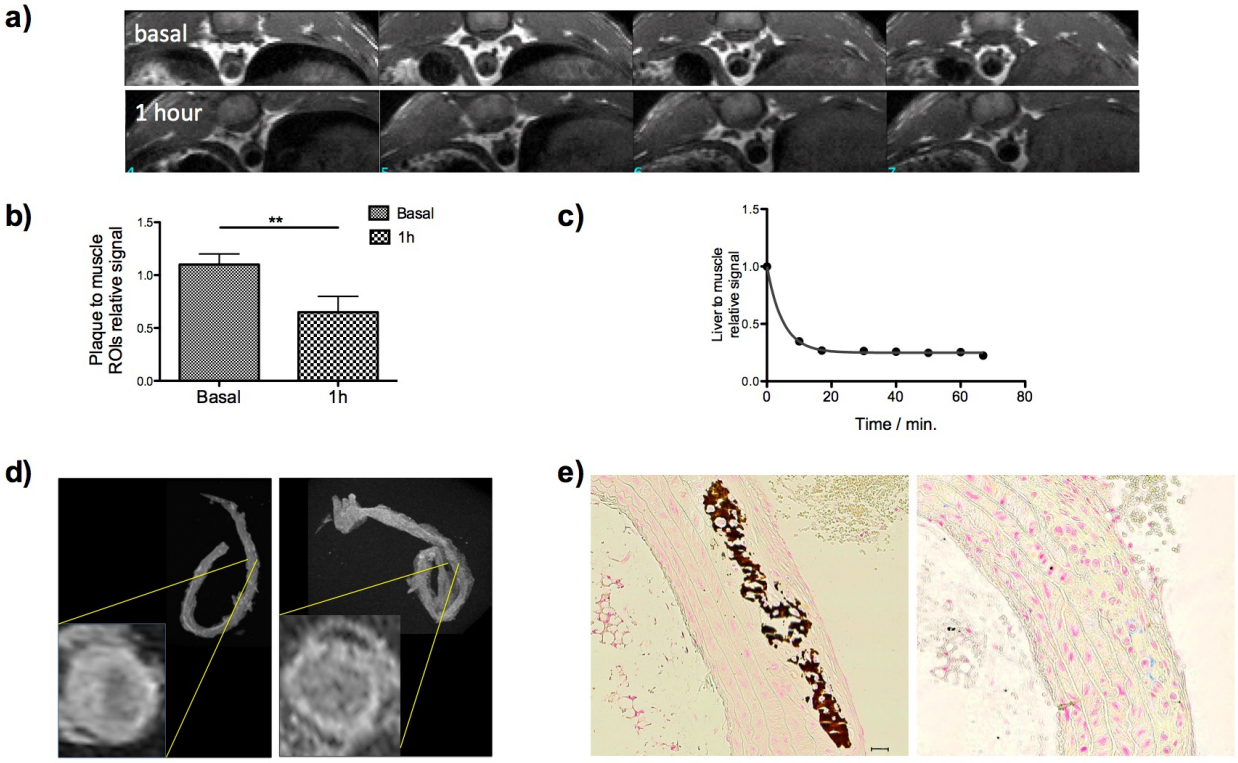

Figure 2. a) *in vivo* MRI of ApoE$^{-/-}$ mouse previous (left) and one hour after the i.v injection of **3** (right); b) Plaque to muscle relative signal intensity previous (basal) and one hour after the i.v injection of **3**; c) Liver to muscle relative signal intensity at different time points after the injection of **3**; d) ex vivo images of the aorta for two mice, without the injection of nanoparticles (left) and one hour after the injection of **3** (right) and e) histology of plaque sections stained with von Kossa and prussian blue, scale bar is 22.2 μm.

Mice, with and without nanoparticles, were sacrificed and their aortas extracted to carry out *ex vivo* MRI. Figure 2d shows the images of the basal and 1 hour post injection where a clear hipointense signal is observed in agreement with *in vivo* data. Finally we carried out histology of the different mice looking for the colocalisation of nanoparticles **3**, macrophages and calcium deposits (Figure 2e, Figure S6 and Figure S7). Three different stainings were used, von Kossa for calcium deposits, F480 for macrophages and Prussian blue for iron. Images clearly show how the iron deposits colocalise with the presence of Ca^{2+} and, only in these spots, with macrophages. In the different images it is clear that the colocalisation of iron with macrophages only occurs when also calcium is present (See Figures S6 and S7). Confirming our hypothesis of plaque accumulation triggered by the calcium binding properties of neridronate-functionalised nanoparticles.

Conclusions

We have demonstrated a new approach on the combined use of bisphosphonates and iron oxide nanoparticles. By microwave technology we synthesised neridronate-functionalised, after a full characterisation we showed their rapid accumulation *in vivo*, when most of the iron oxide nanoparticles for plaque are visualized at least 24 hour after the injection. Thus, the high affinity due to the functional group and specific interaction with

calcium and posterior macrophage uptake of the agglomerates, make our proposal very attractive for translational applications.

Notes and references

[a] Advanced Imaging Unit, Department of Atherothrombosis Imaging and Epidemiology, Fundación Centro Nacional de Investigaciones Cardiovasculares (CNIC) and CIBER de Enfermedades Respiratorias (CIBERES) Melchor Fernández Almagro, 3. 28029 Madrid (Spain).
E-mail: fherranz@cnic.es

[b] Universidad Complutense de Madrid (UCM). Plaza Ramón y Cajal s/n Ciudad Universitaria, 8040 Madrid (Spain).

[c] The Zena and Michael A. Wiener Cardiovascular Institute, Mount Sinai School of Medicine, New York, NY (USA).

This study is supported by a grant from Comunidad de Madrid (S2010/BMD-2326, Inmunothercan-CM), by Fundació La Marató de TV3 (70/C/2012) and by and by Spanish Economy Ministry (MAT2013-47303-P).

Electronic Supplementary Information (ESI) available: Experimental section and supplementary figures. See DOI: 10.1039/c000000x/

1. D.-E. Lee, H. Koo, I.-C. Sun, J. H. Ryu, K. Kim, and I. C. Kwon, *Chem. Soc. Rev.*, 2012, **41**, 2656–72.
2. L. Zhang, W.-F. Dong, and H.-B. Sun, *Nanoscale*, 2013, **5**, 7664–84.
3. C. Gutiérrez-Wing, R. Esparza, C. Vargas-Hernández, M. E. Fernández García, and M. José-Yacamán, *Nanoscale*, 2012, **4**, 2281–7.
4. M. Miyakawa, N. Hiyoshi, M. Nishioka, H. Koda, K. Sato, A. Miyazawa, and T. M. Suzuki, *Nanoscale*, 2014, **6**, 8720–5.
5. E. A. Osborne, T. M. Atkins, D. A. Gilbert, S. M. Kauzlarich, K. Liu, and A. Y. Louie, *Nanotechnology*, 2012, **23**.
6. J. G. Parsons, C. Luna, C. E. Botez, J. Elizalde, and J. L. Gardea-Torresdey, *J. Phys. Chem. Solids*, 2009, **70**, 555–560.
7. X. Liao, J. Zhu, W. Zhong, and H.-Y. Chen, *Mater. Lett.*, 2001, **50**, 341–346.
8. R. M. Wong, D. A. Gilbert, K. Liu, and A. Y. Louie, *ACS Nano*, 2012, **6**, 3461–3467.
9. F. Y. Jiang, C. M. Wang, Y. Fu, and R. C. Liu, *J. Alloys Compd.*, 2010, **503**, L31–L33.
10. W.-W. Wang, Y.-J. Zhu, and M.-L. Ruan, *J. Nanoparticle Res.*, 2006, **9**, 419–426.
11. M. T. Drake, B. L. Clarke, and S. Khosla, *Mayo Clin. Proc.*, 2008, **83**, 1032–45.
12. Y. Lalatonne, C. Paris, J. M. Serfaty, P. Weinmann, M. Lecouvey, and L. Motte, *Chem. Commun. (Camb).*, 2008, 2553–5.
13. L. Sandiford, A. Phinikaridou, A. Protti, L. K. Meszaros, X. Cui, Y. Yan, G. Frodsham, P. A. Williamson, N. Gaddum, R. M. Botnar, P. J. Blower, M. A. Green, and R. T. M. de Rosales, *ACS Nano*, 2013, **7**, 500–12.
14. R. Villa-Bellosta and V. Sorribas, *Arterioscler. Thromb. Vasc. Biol.*, 2009, **29**, 761–6.
15. R. Corti and V. Fuster, *Eur. Heart J.*, 2011, **32**, 1709–1719b.
16. P. R. Moreno, J. Sanz, and V. Fuster, *J. Am. Coll. Cardiol.*, 2009, **53**, 2315–23.
17. D. P. Cormode, T. Skajaa, M. M. van Schooneveld, R. Koole, P. Jarzyna, M. E. Lobatto, C. Calcagno, A. Barazza, R. E. Gordon, P. Zanzonico, E. A. Fisher, Z. A. Fayad, and W. J. M. Mulder, *Nano Lett.*, 2008, **8**, 3715–3723.
18. D. P. Cormode, K. C. Briley-Saebo, W. J. M. Mulder, J. G. S. Aguinaldo, A. Barazza, Y. Ma, E. a Fisher, and Z. a Fayad, *Small*, 2008, **4**, 1437–44.
19. F. M. E. Segers, B. den Adel, I. Bot, L. M. van der Graaf, E. P. van der Veer, W. Gonzalez, I. Raynal, M. de Winther, W. K. Wodzig, R. E. Poelmann, T. J. C. van Berkel, L. van der Weerd, and E. a L. Biessen, *Arterioscler. Thromb. Vasc. Biol.*, 2013, **33**, 1812–9.
20. O. Pascu, E. Carenza, M. Gich, S. Estradé, F. Peiró, G. Herranz, and A. Roig, *J. Phys. Chem. C*, 2012, **116**, 15108–15116.
21. F. Herranz, M. del P. Morales, A. G. Roca, M. Desco, and J. Ruiz-Cabello, *Chem. - A Eur. J.*, 2008, **14**, 9126–30.
22. F. Herranz, M. P. Morales, A. G. Roca, R. Vilar, and J. Ruiz-Cabello, *Contrast Media Mol. Imaging*, 2008, **3**, 215–222.
23. F. Herranz, C. B. Schmidt-Weber, M. H. Shamji, A. Narkus, J. Ruiz-Cabello, and R. Vilar, *Contrast Media Mol. Imaging*, 2012, **7**, 435–9.
24. S. Taktak, R. Weissleder, and L. Josephson, *Langmuir*, 2008, **24**, 7596–8.
25. S. Wagner, J. Schnorr, A. Ludwig, V. Stangl, M. Ebert, B. Hamm, and M. Taupitz, *Int. J. Nanomedicine*, 2013, **8**, 767–79.
26. R. M. Zucker, K. M. Daniel, E. J. Massaro, S. J. Karafas, L. L. Degn, and W. K. Boyes, *Cytometry. A*, 2013.
27. D. G. You, G. Saravanakumar, S. Son, H. S. Han, R. Heo, K. Kim, I. C. Kwon, J. Y. Lee, and J. H. Park, *Carbohydr. Polym.*, 2014, **101**, 1225–33.